

# Sampling-Efficient Mapping of Spherical Images

John Snyder, Don Mitchell

## Abstract

Spherical textures are useful to simulate reflections and to generate arbitrary views from a point. For addressing simplicity, graphics systems require rectangular arrays of texture samples but an infinite variety of functions can be used to map these samples to the sphere. We develop a new metric that measures how well these maps use a given number of samples to provide the greatest worst-case frequency content of the image everywhere over the sphere, or in fact any 3D surface. We show how to calculate this metric locally for any surface parameterization. We also show that the local metric can be conservatively approximated as the larger singular value of the 2D→3D mapping's Jacobian. Using this metric and other important local properties, we compare spherical maps used previously in computer graphics as well as other mappings from cartography, and propose several new, simple mapping functions (dual equidistant and polar-capped maps) that are significantly more efficient. Although we apply the metric to spherical mappings, it is also useful for analyzing the sampling efficiency of texture maps onto any 3D surface. While we consider  $L^\infty$  (worst case) norms on the local metric, others such as the  $L^2$  (average case) are also possible.

**Keywords:** texture mapping, surface parameterization, signal processing, cartography, singular value, Jacobian, metric tensor, Fourier transform

## 1 Introduction

Spherical images representing the radiance field at a point are useful to simulate reflections on shiny surfaces (environment maps) [Bli76, Gre86, Voo94, Hei99] and to produce arbitrary views from a point (spherical panoramas) [Reg94, Che95]. To enhance realism, we expect increasingly widespread use of such spherical images, as well as the use of multiple spherical and hemispherical images per synthetic scene to approximate radiance at many points throughout the environment [Mil98, Hei99, Cab99].

Hardware graphics systems need a simple arrangement of samples from a simple domain to access spherical images and other texture maps. Rectangular arrays of samples (i.e., texture maps) are ubiquitous. This simple structure provides many advantages including locality of reference, simplicity of texel addressing, and ease of filtering for reconstruction. We are not including schemes like spherical wavelets [Sch95a, Sch95b] which exploit local differences in frequency content, but are more complicated to implement in hardware. Still, many functions have been used to map samples from the 2D texture domain to the sphere, including the cube map [Gre86, Reg94, Voo94], OpenGL map [Hae93, Ope92], polar coordinate (latitude/longitude) map [Bli76], and dual stereographic map [Hei99] (called “dual parabolic” in [Hei99]). How should these mappings be compared? Is there anything better?

To answer these questions, we propose the following comparison criteria:

1. *Sampling efficiency*: the mapping function should support the greatest worst-case frequency content in the spherical image using the fewest samples. We prefer a worst-case metric assuming blurry spots in the mapping are undesirable, even if they allow greater fidelity elsewhere. Good worst-case maps also exhibit less variation in sharpness because variations represent an opportunity to improve the metric by redistributing samples. Minimizing texture samples is important to conserve graphics memory and reduce texture bandwidth.
2. *Anisotropy*: isotropic filtering methods (e.g., trilinear interpolation within a MIPMAP) [Wil83] penalize maps having significant anisotropy, since they cause excessive blur in the locally compressed direction. Even hardware having anisotropic filtering capability can not tolerate *unbounded* anisotropy, though isotropy values down to 0.5 are handled with hardware implementations such as Nvidia's TNT [Hüt99].
3. *Simplicity of projection function*: texture coordinate generation by the graphics system should be computable quickly and easily.
4. *Ease of geodesic interpolation*: simple (e.g., linear) interpolation over the domain should closely approximate geodesic interpolation over the sphere.
5. *Ease of creation*: ideally, mappings should be suitable for dynamic creation using the rendering hardware. Note though that maps can be reparameterized using an additional rendering pass over a textured, tessellated sphere.

Another important aspect of mapping functions is the use of map components, such as the six faces of the cube map or two hemispheres in the dual stereographic map. With enough components, or “pieces” in a piecewise map, sampling efficiency can be increased to an asymptotic limit. But there is a price to pay in the form of more complexity in the projection function and reconstruction filtering, reduced locality of reference, and greater difficulty in

Map name	Sampling Requirement	Minimum Isotropy	Map Components
OpenGL	$\infty$	0	1
Cube	24	0.58	6
Dual Stereographic	32	1	2
Lat/Long	19.7	0	1
Dual Equidistant*	19.7	0.64	2
Low Distortion Area Preserving*	19.7	0.29	1
Polar-Capped* (stretch invariant)	14.8	0.71	3
Polar-Capped* (conformal)	16.5	1	3
Polar-Capped* (hexagonally reparameterized)	13.5	0.58	3
Optimal Isometric**	12.57	1	$\infty$
Optimal**	10.9	0.58	$\infty$

**Figure 1: Summary of Spherical Map Properties.** Single-starred maps are new maps described in this paper; double-starred maps are theoretical limits rather than actual maps. Sampling requirement is proportional to the texture area required for a desired frequency content in the worst case; the quantity is formally defined in Section 2.2. Isotropy values closer to 1 are better and represent degree of local conformality (Section 2.3). OpenGL’s map is clearly a poor choice; its infinite sampling requirement simply means that the required number of samples to achieve an increasing frequency content grows faster than quadratically. Latitude/longitude is the most efficient of the maps used previously, but has unbounded anisotropy and thus causes extreme blurring at the poles. Using the new maps, we save 44% over the cube map with no more anisotropy and half as many components (hexagonally reparameterized polar-capped), 48% over the dual stereographic map retaining conformality with one extra component (conformal polar-capped), and 38% over the dual stereographic with somewhat more anisotropy but still using 2 components (dual equidistant).

MIPMAP construction. Equally important, efficiency gains may be lost because of the difficulty in packing many small maps in a texture rectangle without wasting area. For these reasons, only maps having at most a few components are practical.

This paper formally defines sampling efficiency for texture mapping functions over regular 2D lattices by applying results from signal processing [Pet62] and crystallography [Bri56] to spatially-varying mappings. We show that a conservative bound on sampling efficiency is given by considering the largest singular value of the Jacobian over the domain, and also derive efficiency exactly for commonly used maps. Using sampling efficiency and other important properties like anisotropy, we compare maps used previously in computer graphics as well as other mappings from cartography [Rob60,Sny93]. We propose several new mapping functions, including the polar-capped map and dual equidistant map, having superior sampling efficiency and reduced anisotropy. We also provide theoretical limits on the efficiency attainable by any piecewise-differentiable map to the sphere. The results are summarized in Figure 1. The new maps have simple-to-evaluate projection functions that can be implemented using existing hardware to reduce storage and bandwidth requirements and avoid anisotropic blur of spherical images.

## 2 Sampling Efficiency and Other Local Mapping Properties

The *spherical mapping function*,  $\mathbf{S}(u,v)$ , maps 2D points in the plane with parameters  $(u,v)$  to 3D unit-length vectors. Practical mapping functions must cover the sphere from a simple parameter domain,  $\mathbf{D}$ , such as one or more rectangles or perhaps triangles, using a regular sampling pattern such as a rectangular or hexagonal arrangement. Existing graphics systems use rectangular domains and sampling patterns (see Figure 1(a)). Each  $(u,v)$  sample from the tabulated spherical image represents the radiance associated with vector  $\mathbf{S}(u,v)$ , typically stored as an rgb triple.

To analyze frequency content, we will make use of the idea of *circularly bandlimited functions*: functions whose frequency content in any direction is less than a given threshold, or in other words, whose Fourier transform has support inside a disk. This notion of bandlimiting is more appropriate than others like rectangular (separable) ban-

dlimiting, since texture maps can be arbitrarily rotated when projected to the screen. Unlike separable bandlimiting, circular bandlimiting ensures no frequencies are introduced that can alias at other orientations, notably the high diagonal frequencies that occur with separable bandlimiting (see Figure 3a).

Analysis of sampling efficiency is first developed for regular lattices in the plane (Section 2.1). We then extend this analysis to spatially varying mappings by locally projecting the sampling grid onto the tangent plane at each point and applying the same planar analysis (Section 2.2). Section 2.3 presents mathematics for the analysis of local distortion (anisotropy).

## 2.1 Sampling in the Plane

Following [Pet62,Dud84], a regular sampling pattern in the plane can be represented as a *sampling matrix*,  $\mathbf{V} \equiv (\mathbf{v}_1 \ \mathbf{v}_2)$ , where  $\mathbf{v}_1$  and  $\mathbf{v}_2$  are linearly independent vectors to two nearest-neighbor sample locations. For example, isotropic rectangular and hexagonal sampling have the following sampling matrices:

$$\mathbf{V}_{\text{rect}} \equiv \begin{bmatrix} 1 & 0 \\ 0 & 1 \end{bmatrix} \delta, \quad \mathbf{V}_{\text{hex}} \equiv \begin{bmatrix} \sqrt{3}/3 & \sqrt{3}/3 \\ 1 & -1 \end{bmatrix} \delta$$

where  $\delta$  represents the sample spacing. The corresponding sample geometries are shown in Figure 2. Sample locations are derived using  $\mathbf{t} = \mathbf{V}\mathbf{n}$  where  $\mathbf{n} \equiv (n_1, n_2)'$  is a vector of integers (prime denotes transpose).

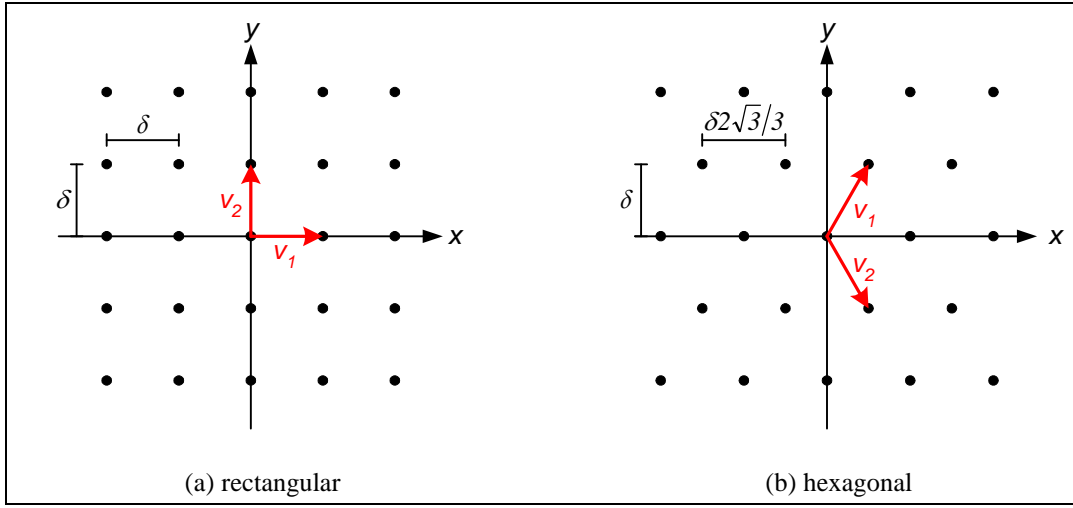


Figure 2: Example Plane Samplings

Denote the continuous signal to be sampled as  $\tilde{\mathbf{f}}(\mathbf{t})$ . The corresponding sampled version,  $\mathbf{f}(\mathbf{n})$ , is given by

$$\mathbf{f}(\mathbf{n}) \equiv \tilde{\mathbf{f}}(\mathbf{t}) = \tilde{\mathbf{f}}(\mathbf{V}\mathbf{n}).$$

Taking the Fourier transform of  $\tilde{\mathbf{f}}$  and then its inverse, we obtain

$$\begin{aligned} \tilde{\mathbf{F}}(\boldsymbol{\Omega}) &\equiv \int_{-\infty}^{+\infty} \tilde{\mathbf{f}}(\mathbf{t}) \exp(-i\boldsymbol{\Omega}'\mathbf{t}) d\mathbf{t} \\ \tilde{\mathbf{f}}(\mathbf{t}) &= \frac{1}{4\pi^2} \int_{-\infty}^{+\infty} \tilde{\mathbf{F}}(\boldsymbol{\Omega}) \exp(i\boldsymbol{\Omega}'\mathbf{t}) d\boldsymbol{\Omega} \end{aligned}$$

where  $\boldsymbol{\Omega} \equiv (\boldsymbol{\Omega}_x \ \boldsymbol{\Omega}_y)'$  is in units of radians per unit length. Doing the same for the discrete signal,  $\mathbf{f}$ , we get

$$\begin{aligned} \mathbf{F}(\boldsymbol{\omega}) &\equiv \sum_{\mathbf{n}} \mathbf{f}(\mathbf{n}) \exp(-i\boldsymbol{\omega}'\mathbf{n}) \\ \mathbf{f}(\mathbf{n}) &= \frac{1}{4\pi^2} \int_{-\pi}^{+\pi} \mathbf{F}(\boldsymbol{\omega}) \exp(i\boldsymbol{\omega}'\mathbf{n}) d\boldsymbol{\omega} \end{aligned} \tag{1}$$

where  $\boldsymbol{\omega} \equiv (\omega_x \ \omega_y)'$  is in units of radians. So

$$\mathbf{f}(\mathbf{n}) = \tilde{\mathbf{f}}(\mathbf{V}\boldsymbol{\Omega}) = \frac{1}{4\pi^2} \int_{-\infty}^{+\infty} \tilde{\mathbf{F}}(\boldsymbol{\Omega}) \exp(i\boldsymbol{\Omega}'\mathbf{V}\mathbf{n}) d\boldsymbol{\Omega}.$$

Substituting  $\boldsymbol{\omega} = \mathbf{V}'\boldsymbol{\Omega}$  yields

$$\mathbf{f}(\mathbf{n}) = \frac{1}{4\pi^2} \int_{-\infty}^{+\infty} \frac{1}{|\det \mathbf{V}|} \tilde{\mathbf{F}}(\mathbf{V}'^{-1}\boldsymbol{\omega}) \exp(i\boldsymbol{\omega}'\mathbf{n}) d\boldsymbol{\omega}.$$

The double integral in the  $(\omega_x \ \omega_y)$ -plane can be broken into an infinite sum of integrals each covering a square area of  $4\pi^2$ :

$$\mathbf{f}(\mathbf{n}) = \frac{1}{4\pi^2} \sum_{k_x} \sum_{k_y} \int_{-\pi+2\pi k_x}^{\pi+2\pi k_x} \int_{-\pi+2\pi k_y}^{\pi+2\pi k_y} \frac{1}{|\det \mathbf{V}|} \tilde{\mathbf{F}}(\mathbf{V}'^{-1}\boldsymbol{\omega}) \exp(i\boldsymbol{\omega}'\mathbf{n}) d\boldsymbol{\omega}$$

Replacing  $\omega_x$  by  $\omega_x - 2\pi k_x$  and  $\omega_y$  by  $\omega_y - 2\pi k_y$  removes the dependence of integration limits on  $\mathbf{k}$ :

$$\mathbf{f}(\mathbf{n}) = \frac{1}{4\pi^2} \sum_{k_x} \sum_{k_y} \int_{-\pi}^{+\pi} \int_{-\pi}^{+\pi} \frac{1}{|\det \mathbf{V}|} \tilde{\mathbf{F}}(\mathbf{V}'^{-1}(\boldsymbol{\omega} - 2\pi\mathbf{k})) \exp(i\boldsymbol{\omega}'\mathbf{n}) \exp(i2\pi\mathbf{k}'\mathbf{n}) d\boldsymbol{\omega} \quad (2)$$

The second exponential term is always 1 since  $\mathbf{k}$  is an integer-valued vector. Then equating (1) and (2) implies that

$$\begin{aligned} \mathbf{F}(\boldsymbol{\omega}) &= \frac{1}{|\det \mathbf{V}|} \sum_{\mathbf{k}} \tilde{\mathbf{F}}(\mathbf{V}'^{-1}(\boldsymbol{\omega} - 2\pi\mathbf{k})), \quad \text{or} \\ \mathbf{F}(\mathbf{V}'\boldsymbol{\Omega}) &= \frac{1}{|\det \mathbf{V}|} \sum_{\mathbf{k}} \tilde{\mathbf{F}}(\boldsymbol{\Omega} - \mathbf{U}\mathbf{k}) \end{aligned}$$

where  $\mathbf{U} \equiv 2\pi\mathbf{V}'^{-1}$ .

$\mathbf{F}(\mathbf{V}'\boldsymbol{\Omega})$  is a periodic extension of  $\tilde{\mathbf{F}}(\boldsymbol{\Omega})$  where the periodicity is described by the matrix  $\mathbf{U} = (\mathbf{u}_1 \ \mathbf{u}_2)$ . Since  $\mathbf{F}(\boldsymbol{\omega})$  is periodic in  $\omega_x$  and  $\omega_y$  with period  $2\pi$ ,  $\mathbf{F}(\mathbf{V}'(\boldsymbol{\Omega} + \mathbf{U}\mathbf{k})) = \mathbf{F}(\mathbf{V}'\boldsymbol{\Omega} + 2\pi\mathbf{k}) = \mathbf{F}(\mathbf{V}'\boldsymbol{\Omega})$ . Thus the Fourier transform of the discrete signal has a periodicity matrix related to the original sampling matrix via  $\mathbf{U} \equiv 2\pi\mathbf{V}'^{-1}$ . To eliminate aliasing, we need to bandlimit  $\tilde{\mathbf{f}}(\mathbf{t})$  such that its Fourier transform,  $\tilde{\mathbf{F}}(\boldsymbol{\Omega})$ , is zero outside a finite region in frequency space. The region is chosen so as to have no overlap between neighboring periodically repeated parts or *tiles* of  $\mathbf{F}(\mathbf{V}'\boldsymbol{\Omega})$ . For the rectangular and hexagonal sampling matrix examples, we have

$$\mathbf{U}_{rect} \equiv \begin{bmatrix} 2 & 0 \\ 0 & 2 \end{bmatrix} \frac{\pi}{\delta}, \quad \mathbf{U}_{hex} \equiv \begin{bmatrix} \sqrt{3} & \sqrt{3} \\ 1 & -1 \end{bmatrix} \frac{\pi}{\delta}$$

with frequency space tiles shown in Figure 3.

For such a bandlimited function, inside the periodic tile containing the origin, called the *baseband*,  $\mathbf{B}$ , the continuous and discrete Fourier transformed functions are related via

$$\mathbf{F}(\mathbf{V}'\boldsymbol{\Omega}) = \frac{1}{|\det \mathbf{V}|} \tilde{\mathbf{F}}(\boldsymbol{\Omega})$$

implying we can reconstruct such bandlimited functions exactly from the discrete samples. In fact, the reconstruction is given by

$$\tilde{\mathbf{f}}(\mathbf{t}) = \frac{|\det \mathbf{V}|}{4\pi^2} \sum_{\mathbf{n}} \mathbf{f}(\mathbf{n}) \int_{\mathbf{B}} \exp(i\boldsymbol{\Omega}'(\mathbf{t} - \mathbf{V}\mathbf{n})) d\boldsymbol{\Omega}.$$

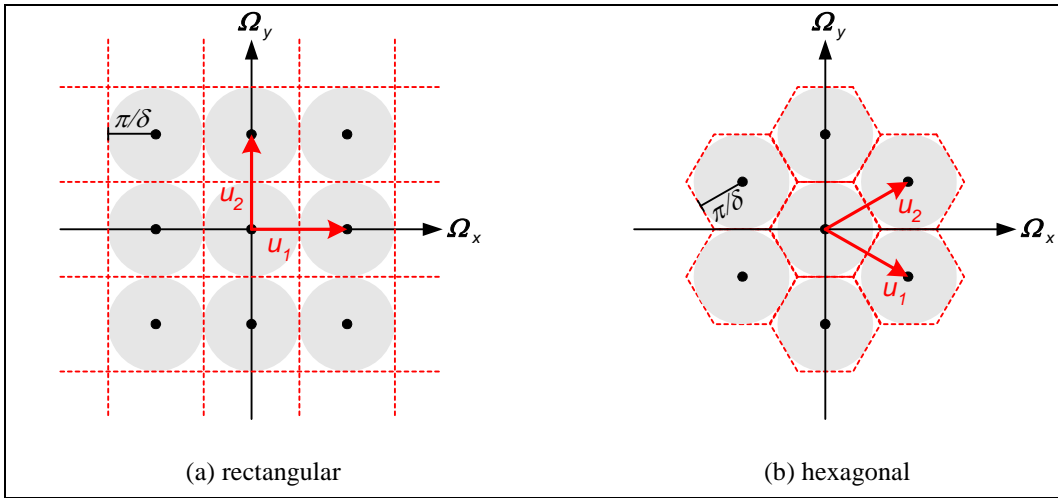


**Figure 3: Fourier transform of discrete signals from example sampling matrices.** Note that both rectangular and hexagonal sampling provide for frequencies up to  $\pi/\delta$  in all directions without aliasing. In other words, a frequency radius of  $\pi/\delta$  is the largest for an inscribed circle in each periodic tile. Interestingly though, hexagonal sampling requires 13.4% fewer samples to accomplish this, since the circles are packed more tightly in each hexagonal tile, while the square tiles waste space on diagonal frequencies outside the frequency radius. In fact, it can be shown that hexagonal sampling is optimal, in the sense that it has the smallest sampling density of any regular pattern to achieve a given frequency radius.

Given a sampling matrix  $\mathbf{V}$ , we can calculate the radius of the largest inscribed circle in the baseband of its frequency plane; that is, the maximum frequency content in all directions that a circularly bandlimited periodic signal sampled using  $\mathbf{V}$  can support. This is calculated by computing  $\mathbf{U} \equiv 2\pi\mathbf{V}^{-1} = (\mathbf{u}_1 \ \mathbf{u}_2)$  and finding half the minimum distance of the origin to the vectors  $n_1\mathbf{u}_1 \pm n_2\mathbf{u}_2$ , for integers  $n_1$  and  $n_2$  not both zero. We thus define the *sampling spectral radius*,  $\Delta$ , of the sampling matrix  $\mathbf{V}$  via

$$\begin{aligned} \Delta &\equiv 1/2 \min_{(n_1, n_2) \neq (0,0)} (\|n_1\mathbf{u}_1 - n_2\mathbf{u}_2\|) \\ &= \frac{\pi}{|\det \mathbf{V}|} \min_{(n_1, n_2) \neq (0,0)} (\|n_1\mathbf{v}_1 - n_2\mathbf{v}_2\|) \end{aligned} \quad (3)$$

For the rectangular and hexagonal example samplings,  $\Delta = \pi/\delta$ . It can be shown ([Pet62]) that among all sampling matrices having a given sampling spectral radius, the most efficient is always isotropic hexagonal sampling, in that it covers the greatest area with the fewest samples. Sampling density can be measured by  $d \equiv 1/|\det \mathbf{V}|$ , for which our example sampling matrices yield  $d_{rect} = \delta^2$  and  $d_{hex} = 2\sqrt{3}/3 \delta^2$ .

## 2.2 Mapped Sampling

We are interested in frequency content on the sphere, not the plane. We therefore locally apply the previous section's analysis of regular sampling patterns in 2D, and examine the worst-case frequency content anywhere in the map's image. For rectangular sampling, squares in parameter space are mapped into "quadrilateral" regions on the sphere, as shown in **Figure 4**. We can approximate the spherical samples in the neighborhood of  $\mathbf{S}(u, v)$  by 2D points projected to the tangent plane there.

Let  $\mathbf{S}_u(u, v) \equiv \partial\mathbf{S}/\partial u(u, v)$  and  $\mathbf{S}_v(u, v) \equiv \partial\mathbf{S}/\partial v(u, v)$ . Then an orthonormal basis for the tangent space is given by  $(\mathbf{T}_1 \ \mathbf{T}_2)$

$$\begin{aligned} \mathbf{T}_1(u, v) &\equiv \frac{\mathbf{S}_u}{\|\mathbf{S}_u\|} \\ \mathbf{T}_2(u, v) &\equiv \frac{(\mathbf{S}_u \cdot \mathbf{S}_u)\mathbf{S}_v - (\mathbf{S}_u \cdot \mathbf{S}_v)\mathbf{S}_u}{\|\mathbf{S}_u\|^2} \end{aligned}$$

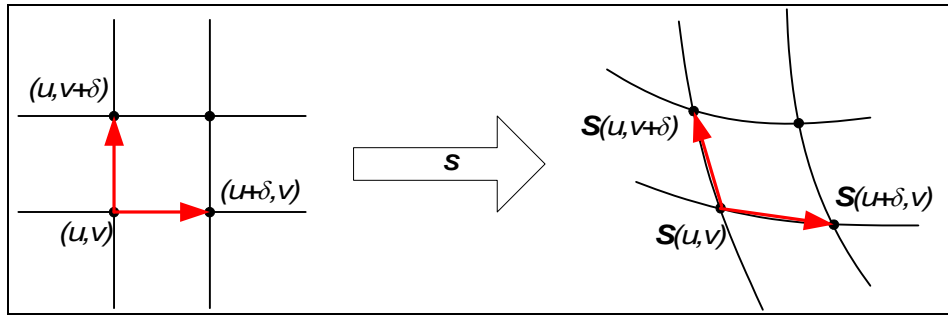


Figure 4: Mapped Rectangular Sampling.

where  $\tau(u, v) \equiv \sqrt{(\mathbf{S}_u \cdot \mathbf{S}_u)(\mathbf{S}_v \cdot \mathbf{S}_v) - (\mathbf{S}_u \cdot \mathbf{S}_v)^2}$  represents the differential area at  $(u, v)$ . Letting  $\mathbf{J}(u, v) \equiv (\mathbf{S}_u \ \mathbf{S}_v)$ , the approximation

$$\mathbf{S}((u, v) + (\dot{u}, \dot{v})) - \mathbf{S}(u, v) \approx \mathbf{J}(\dot{u}, \dot{v}) \quad (4)$$

is good for small  $\|(\dot{u}, \dot{v})\|$ , becoming exact in the limit as the length of the perturbation reaches 0. Since the Jacobian  $\mathbf{J}$  maps perturbations in any domain direction to the tangent plane, it can be thought of as a “local” sampling matrix. Alternatively, we can think of the Jacobian as distorting what was formerly simple rectangular sampling in the plane. To derive a 2D sampling matrix, we must project the Jacobian into the plane using the orthonormal basis  $(\mathbf{T}_1 \ \mathbf{T}_2)$ , a pure rotation which preserves the sampling properties. Defining  $\mathbf{K}$  as the resulting transformed Jacobian:

$$\mathbf{K}(u, v) \equiv (\mathbf{T}_1(u, v) \ \mathbf{T}_2(u, v))' \mathbf{J}(u, v) = \frac{1}{\|\mathbf{S}_u\|} \begin{bmatrix} \mathbf{S}_u \cdot \mathbf{S}_u & \mathbf{S}_u \cdot \mathbf{S}_v \\ 0 & \tau \end{bmatrix}$$

For rectangular sampling with spacing  $\delta$ , the *local sampling matrix* mapped by  $\mathbf{S}$  is then given by  $\mathbf{V} = \delta \mathbf{K}$ .

We can now analyze the spectral radius determined by  $\mathbf{V}$  at any point  $(u, v)$  as if  $\mathbf{S}$  were everywhere equal to the local approximation in (4). By selecting the minimum sampling spectral radius for any point in  $\mathbf{D}$ , we determine the highest permissible frequency,  $\Delta^*$ , in a circularly bandlimited function rectangularly sampled with spacing  $\delta$  using the given mapping function. Substituting the local sampling matrix into the definition of sampling spectral radius (3) and simplifying yields the *local sampling spectral radius*  $\Delta(u, v)$ :

$$\Gamma(u, v) \equiv \frac{\tau(u, v)}{\min_{(n_1, n_2) \neq (0, 0)} (\|n_1 \mathbf{S}_u + n_2 \mathbf{S}_v\|)}$$

$$\Delta(u, v) \equiv \frac{\pi}{\delta \Gamma(u, v)}$$

where  $n_1$  and  $n_2$  are integers. We call  $\Gamma$  the *local sampling spectral stretch* of the mapping. An algorithm to compute  $\Gamma$  by searching only a finite 1D subset of integer lattice is contained in Appendix 8. The minimum local sampling spectral radius over the parameter domain,  $\Delta^*$ , is then defined via

$$\Gamma^* \equiv \max_{(u, v) \in \mathbf{D}} \Gamma(u, v)$$

$$\Delta^* \equiv \min_{(u, v) \in \mathbf{D}} \Delta(u, v) = \frac{\pi}{\delta \Gamma^*}$$

As expected, for a given mapping function, we can make  $\Delta^*$  arbitrarily large by reducing  $\delta$ , essentially, by adding more samples. The concept of the sampling stretch can also be generalized to sampling strategies in the domain other than rectangular, by transforming the domain’s original 2D sampling matrix (rather than  $\mathbf{I}\delta$ ) using  $\mathbf{K}$  and then finding its sampling spectral radius. We concentrate on rectangular sampling because of its simplicity, efficiency, and widespread use in graphics systems.

We can now compare efficiencies of various mappings by fixing the sampling spectral radius and determining the number of samples (or equivalently, the sample spacing  $\delta$ ) required to generate that desired frequency content. The number of samples required to sample the sphere (or indeed any desired portion of the image of any mapping function) is given by

$$N \equiv \frac{A}{\delta^2} = \frac{A}{\left(\frac{\pi}{\Gamma^* \Delta^*}\right)^2} = (A\Gamma^{*2}) \left(\frac{\Delta^*}{\pi}\right)^2$$

where  $A$  is the area of the domain  $\mathbf{D}$ . Defining the *sampling efficiency* of a mapping,  $M_{\mathbf{S}}^{-1} \equiv 1/\left(A\Gamma^{*2}\right)$ , then implies that the number of samples required to achieve a minimum spectral radius  $\Delta^*$  is  $N = \left(\Delta^*/\pi\right)^2 / M_{\mathbf{S}}^{-1}$ . Higher efficiency means fewer samples required for a given spectral radius everywhere in  $\mathbf{D}$ . We call the reciprocal of sampling efficiency the *sampling requirement*, defined

$$M_{\mathbf{S}} \equiv A\Gamma^{*2}.$$

### 2.3 Local Distortion Analysis

For hundreds of years, the field of cartography has studied spherical mappings and their properties. In 1881, Tissot analyzed the local deformation induced by spherical mappings in his *Mémoire sur la représentation des surfaces et les projections des cartes géographiques*. While cartography seeks to optimize perceptual reproduction of the Earth's surface on a flat projection rather than sampling efficiency, its tools of analysis and catalog of maps are nonetheless useful for our purposes. Using Tissot's analysis, a mapping function locally transforms an infinitesimal circle into a general ellipse, with eccentricity and rotation that can be determined from the Jacobian of the mapping. The lengths of the major and minor axes of this ellipse,  $\lambda_1$  and  $\lambda_2$ , are given by the singular values of the Jacobian

$$\lambda_1^2(u, v) \equiv \frac{(a+c) + \sqrt{(a-c)^2 + 4b^2}}{2}$$

$$\lambda_2^2(u, v) \equiv \frac{(a+c) - \sqrt{(a-c)^2 + 4b^2}}{2}$$

where  $a(u, v) \equiv \mathbf{S}_u \cdot \mathbf{S}_u$ ,  $b(u, v) \equiv \mathbf{S}_u \cdot \mathbf{S}_v$ , and  $c(u, v) \equiv \mathbf{S}_v \cdot \mathbf{S}_v$  are the entries in the symmetric metric tensor  $\mathbf{J}^T \mathbf{J}$ . So  $\lambda_1$  represents the maximum local stretch or length of the longest vector mapped from the set of unit tangent vectors in the domain, and  $\lambda_2$  the maximum compression or length of the shortest mapped vector. The singular values are related to the differential area via  $\tau = \lambda_1 \lambda_2$ . We also define the *isotropy* of the mapping,  $\alpha \equiv \lambda_2 / \lambda_1$  where  $0 \leq \alpha \leq 1$  whose closeness to 0 is useful for measuring the severity of artifacts from MIPMAP filtering. We call  $1/\alpha$  the *anisotropy*.

Mapping functions can be categorized by their local properties as follows:

$$\begin{aligned} \text{isometric} &\Rightarrow \lambda_1(u, v) = \lambda_2(u, v) = \eta \\ \text{conformal} &\Rightarrow \lambda_1(u, v) = \lambda_2(u, v) \\ \text{equivalent or area-preserving} &\Rightarrow \lambda_1(u, v) \lambda_2(u, v) = \eta \\ \text{stretch-preserving} &\Rightarrow \lambda_1(u, v) = \eta \end{aligned}$$

where  $\eta$  is a constant and the properties are for all  $(u, v) \in \mathbf{D}$ . The last category is not one used formally in cartography, but will be useful in the next section. The first is not possible for smooth spherical mapping functions but only for mappings to developable surfaces. Conformal mappings in computer graphics are discussed in [Fiu87].

There is a close relation between the sampling spectral stretch of a mapping  $\Gamma$  and its largest singular value  $\lambda_1$ , although the two are not identical. We have  $\Gamma \leq \lambda_1$  because

$$\Gamma = \frac{\tau}{\min_{(n_1, n_2) \neq (0,0)} (\|n_1 \mathbf{S}_u + n_2 \mathbf{S}_v\|)} = \frac{\lambda_1 \lambda_2}{\min_{(n_1, n_2) \neq (0,0)} (\|n_1 \mathbf{S}_u + n_2 \mathbf{S}_v\|)} = \lambda_1 \frac{\min_{\|(x,y)\|=1} (\|x \mathbf{S}_u + y \mathbf{S}_v\|)}{\min_{(n_1, n_2) \neq (0,0)} (\|n_1 \mathbf{S}_u + n_2 \mathbf{S}_v\|)} \leq \lambda_1$$

and since  $\|(n_1, n_2)\| \geq 1$  for integers not both 0. Thus  $\lambda_1$  is a conservative estimate for the more difficult to calculate  $\Gamma$ ; i.e., when substituted for  $\Gamma$  provides a lower bound on the sampling efficiency. Also, in the case of an orthogonal parameterization (in which  $\mathbf{b} \equiv \mathbf{S}_u \cdot \mathbf{S}_v = 0$ ),  $\Gamma = \lambda_1$  and

$$\lambda_1 = \max(\|\mathbf{S}_u\|, \|\mathbf{S}_v\|)$$

$$\lambda_2 = \min(\|\mathbf{S}_u\|, \|\mathbf{S}_v\|)$$

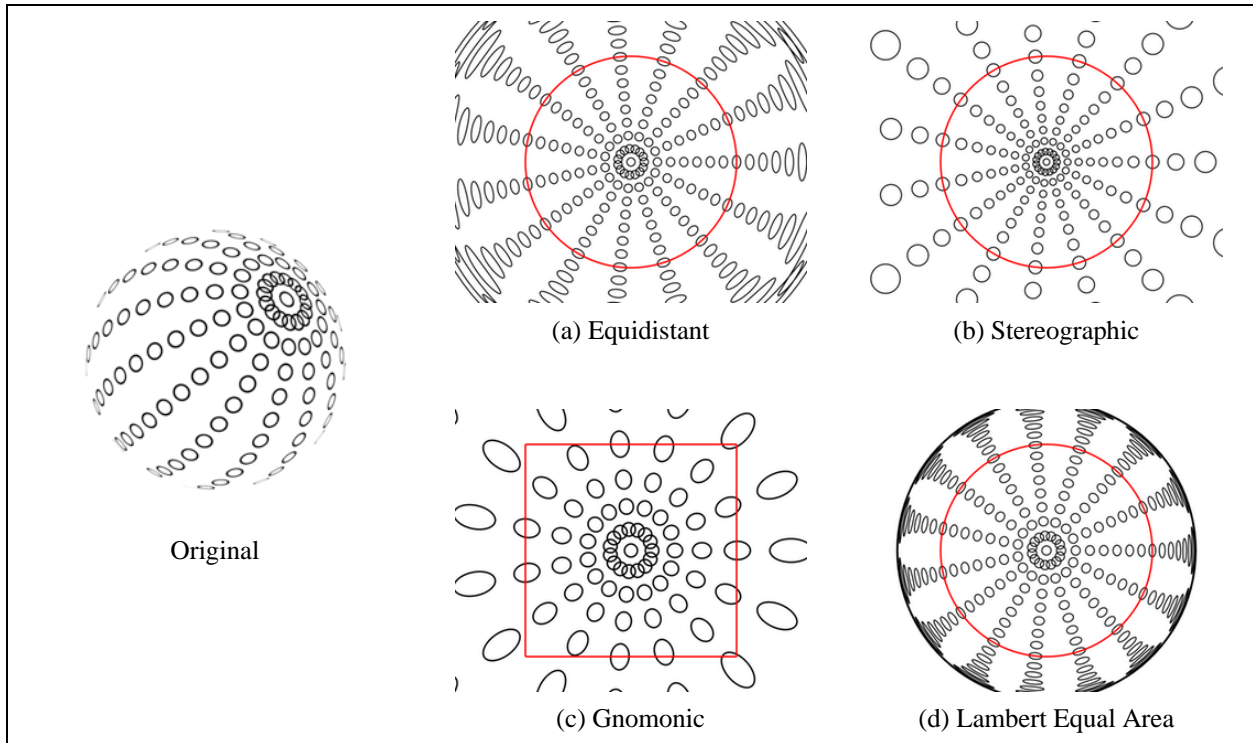


**Figure 5: Azimuthal Projections:** Spherical circles having a radius of  $3.5^\circ$  and arranged at intervals of  $12.5^\circ$  in latitude and  $22.5^\circ$  in longitude are projected back into parameter space using the four azimuthal projections. The red circle represents the extent of a hemisphere. For the gnomonic map, which is unable to represent the entire hemisphere in a finite domain, a single face from the cube map is shown in red. Note that greater mapping stretch is indicated by smaller projected circles in the domain since we are projecting constant size spherical circles back into parameter space.

Finally, note that the sampling requirement satisfies  $M_S \leq \rho/k$  where  $\rho$  is the surface area of the image of the mapping function over the domain  $\mathcal{D}$  and  $k \equiv 2\sqrt{3}/3$ . This is because there is no more efficient sampling than isotropic hexagonal sampling [Pet62], for which the relation can be easily verified for  $\mathbf{K}(u, v) = \mathbf{V}_{\text{hex}}$ . For an isometric map,  $M_S = \rho$ .

### 3 Spherical Maps and Their Efficiencies

We analyze the sampling efficiency and local properties of some simple projections from cartography [Rob60, pages 66-120], some of which have appeared in computer graphics. Where possible, we retain the terminology of cartography and relate it to that used in computer graphics.

#### 3.1 Azimuthal Projections

Azimuthal projections transform the sphere into a tangent or intersecting plane such that parallels (lines of constant latitude on the earth) are projected to circles.<sup>1</sup> Mathematically, these projections may be modeled as

$$\mathbf{S}(u, v) = \left( (u/r) \sin \theta(r), (v/r) \sin \theta(r), \cos \theta(r) \right), \quad r = \sqrt{u^2 + v^2}, \quad u, v \in [-r^*, r^*] \quad (5)$$

where  $\theta(r) \in [0, \pi]$  arbitrarily reparameterizes the parallel spacing, and where  $\theta = 0$  and  $\theta = \pi$  represent the poles. Figure 6 summarizes the four most important azimuthal projections from cartography: gnomonic, stereographic, Lambert equal area, and equidistant, which are illustrated in **Figure 5**.

The *gnomonic* map projects the sphere onto a plane tangent to it, using a perspective transformation that looks directly at the point of tangency. It is the projection used in the “cube map” spherical image [Gre86, Reg94], for each of the six faces of the cube. The gnomonic map projects great circles on the sphere to straight lines in the map

<sup>1</sup> Of course the coordinate system can be arbitrarily rotated so as to be centered about any point rather than the usual north or south pole of the earth.

domain, an advantageous property for texture coordinate interpolation. Gnomonic maps can also be directly produced using the perspective projection of the rendering hardware. Note that the gnomonic map requires the entire real plane to parameterize a hemisphere. The *stereographic* map is a conformal map that also has the property that circles on the sphere project to circles in the domain. [Hei99] proposes dual stereographic maps, one for each hemisphere, to parameterize environment maps. The *Lambert equal area* map is an area-preserving map also called the “gazing ball” or OpenGL map [Ope92]. Finally, the *equidistant* map is a stretch-preserving map that also preserves distances to the pole. Although it has not been used in computer graphics, its sampling efficiency exceeds that of the other azimuthal projections, as we will demonstrate shortly.

	Equidistant	Gnomonic	Stereographic	Lambert Equal Area
$\theta(r)$	$(\pi/2)r$	$\cos^{-1}\left(\sqrt{1/(r^2+1)}\right)$	$\cos^{-1}\left((1-r^2)/(1+r^2)\right)$	$\cos^{-1}(1-r^2)$
properties	stretch-preserving	projects great circles to lines	conformal, projects circles to circles	area-preserving
$r^*$ covering hemisphere	$[0, 1]$	$[0, \infty]$	$[0, 1]$	$[0, 1]$
$r^*$ covering sphere	$[0, 2]$	–	$[0, \infty]$	$[0, \sqrt{2}]$
$r(\theta)$	$2\theta/\pi$	$\tan \theta$	$\tan(\theta/2)$	$\sqrt{1-\cos \theta}$
$\sin \theta$	$\sin((\pi/2)r)$	$r/\sqrt{r^2+1}$	$2r/(1+r^2)$	$r\sqrt{2-r^2}$
$\cos \theta$	$\cos((\pi/2)r)$	$\sqrt{1/(r^2+1)}$	$(1-r^2)/(1+r^2)$	$1-r^2$
$\lambda_1(\theta)$	$\pi/2$	$\cos \theta$	$1+\cos \theta$	$2/\sqrt{1+\cos \theta}$
$\lambda_2(\theta)$	$(\pi/2)\text{sinc } \theta$	$\cos^2 \theta$	$1+\cos \theta$	$\sqrt{1+\cos \theta}$
$\alpha(\theta)$	$\text{sinc } \theta$	$\cos \theta$	1	$(1+\cos \theta)/2$
$\tau(\theta)$	$(\pi/2)^2 \text{sinc } \theta$	$\cos^3 \theta$	$(1+\cos \theta)^2$	2
$\lambda_1^*(\theta)$	$\pi/2$	1	2	$2/\sqrt{1+\cos \theta}$
$M_S(\theta)$	$4\theta^2$	$4 \tan^2 \theta$	$16 \tan^2(\theta/2)$	$16 \tan^2(\theta/2)$
inverse map	$f = (\pi/2)\text{sinc}(\cos^{-1} z)$ $u = x/f$ $v = y/f$	$u = x/z$ $v = y/z$	$u = x/(1+z)$ $v = y/(1+z)$	$u = x/\sqrt{1+z}$ $v = y/\sqrt{1+z}$

**Figure 6: Table of Mathematical Properties of Azimuthal Projections.** We define  $\text{sinc } \theta \equiv \sin \theta/\theta$ . Note that the local properties do not vary as a function of the direction of the vector  $(u, v)$ , only as a function of its length  $r$  or equivalently,  $\theta$ . The maximum larger singular value,  $\lambda_1^*$ , and the sampling requirement,  $M_S$ , are taken over the portion of the sphere from  $[0, \theta]$ , thus allowing analysis of parts of the sphere from the pole to any parallel, such as the hemisphere ( $\theta=\pi/2$ ). The inverse maps implement the texture coordinate generation required by graphics systems.

The local distortion properties of the four maps can be straightforwardly derived from (5) using the respective definition of  $\theta(r)$  from the table. To derive the sampling efficiency of these maps, first note that the singular values of the projections are invariant over any circle in the domain centered at the origin,  $\mathbf{D}_r \equiv \{(u, v) \mid u^2 + v^2 = r^2\}$ . It can also be shown that the metric tensor entries are given by

$$a = u^2 d + e, \quad c = v^2 d + e, \quad |b| = uv d$$

where

$$\mathbf{d} \equiv \frac{\lambda_1^2 - \lambda_2^2}{r^2}, \quad \mathbf{e} \equiv \lambda_2^2$$

and  $\mathbf{d}, \mathbf{e} \geq 0$ . Then sampling spectral stretch  $\Gamma^{-2}$  is given by

$$\Gamma^2 = \frac{\lambda_1^2 \lambda_2^2}{\min_{(n_1, n_2) \neq (0,0)} (n_1^2 \mathbf{a} - 2n_1 n_2 |\mathbf{b}| + n_2^2 \mathbf{c})}$$

Maximizing  $\Gamma^2$  over a domain circle  $\mathbf{D}_r$  requires minimizing the denominator above, since the numerator is invariant over  $\mathbf{D}_r$ ; denote this maximum as  $\Gamma_r^2$ . Examining the denominator, which we denote  $\gamma^2$ ,

$$\begin{aligned} \gamma^2 &\equiv \min_{(n_1, n_2) \neq (0,0)} (n_1^2 \mathbf{a} - 2n_1 n_2 |\mathbf{b}| + n_2^2 \mathbf{c}) \\ &= \min_{(n_1, n_2) \neq (0,0)} ((n_1^2 + n_2^2) \mathbf{e} + (n_1^2 u^2 - 2n_1 n_2 uv + n_2^2 v^2) \mathbf{d}) \\ &= \min_{(n_1, n_2) \neq (0,0)} ((n_1^2 + n_2^2) \mathbf{e} + (n_1 u - n_2 v)^2 \mathbf{d}) \end{aligned}$$

It can be seen that the minimum value of  $\gamma^2$  over  $\mathbf{D}_r$ , which we denote  $\gamma_r^2$ , occurs at  $(n_1, n_2) = (0,1)$ ,  $(u, v) = (r, 0)$  (or equivalently at  $(n_1, n_2) = (1,0)$ ,  $(u, v) = (0, r)$ ), since  $\mathbf{d}, \mathbf{e} \geq 0$  and the integer factors can not both be zero. Thus,  $\gamma_r^2 = \mathbf{e} = \lambda_2^2(r)$  so  $\Gamma_r^2 = \lambda_1^2(r)$ ; in words, *for any azimuthal projection, the maximum spectral stretch over a circle centered at the pole is the same as the larger singular value anywhere on the circle.*

The sampling requirement tabulated in Figure 6 is then given by the domain area times the square of the maximum  $\lambda_1$ ; i.e.,

$$\begin{aligned} M_S(\theta) &= 4r^2(\theta) \lambda_1^{*2}(\theta) \quad \text{where} \\ \lambda_1^*(\theta) &\equiv \max_{\varphi \in [0, \theta]} \lambda_1(\varphi) \end{aligned}$$

While this domain is properly a disk in 2D, we take its area as  $4r^2$  rather than  $\pi r^2$  to calculate efficiency with the assumption that the disk samples must be embedded in a square to allow a practical indexing scheme. Because the equidistant map is stretch-invariant, its maximum spectral stretch does not depend on  $r$ , and thus has optimal sampling efficiency among all azimuthal projections.

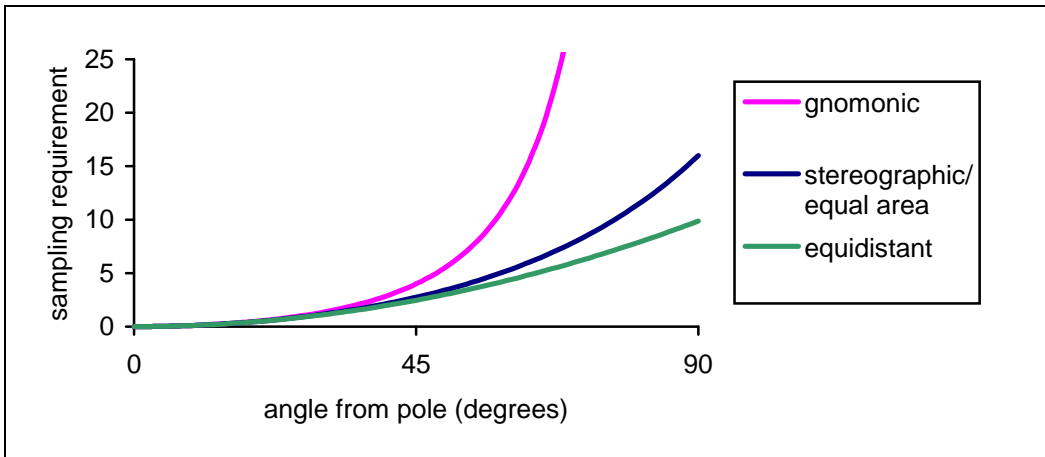


**Figure 7: Sampling Requirements of Azimuthal Maps as a Function of Angular Coverage.**

Figure 7 graphs sampling requirements of the various azimuthal maps for portions of the sphere up to a hemisphere. A single gnomonic map can not encompass the entire hemisphere; its sampling requirement becomes unbounded. The equidistant map has sampling requirement  $M_S(\pi/2) = 4(\pi/2)^2 \approx 9.87$  while both the stereographic and equal area maps have  $M_S(\pi/2) = 16 \tan^2(\pi/4) = 16$ . To cover the sphere, it is more efficient to use two maps each covering a hemisphere (called a *dual projection*) rather than a single one covering the entire sphere. In fact, both the stereographic and equal area maps have unbounded sampling requirement when used to cover the entire sphere, but for different reasons. The stereographic projection requires the entire real plane to cover the sphere

while the equal area projection has unbounded spectral stretch at the opposite pole. Interestingly, the use of six gnomonic maps for each face of the cube provides a sampling requirement of 24, better than dual equal area or stereographic maps with a sampling requirement of 32, but less good than dual equidistant maps at about 19.74.<sup>2</sup> For reference, these numbers can be compared to the surface area of the unit sphere,  $\rho = 4\pi \approx 12.57$ . We will see in Section 4 how to further improve this advantage of the equidistant map.

It is easy to show that the sampling efficiency of a set of gnomonic maps, one for each face of a polyhedron circumscribing the sphere, is given by the surface area of that polyhedron. This is because the maximum spectral stretch of the gnomonic map is 1 and occurs at the center (pole) of the projection within each face; the domain area is the same as the area of the face. The following table lists the sampling requirements,  $M_s$ , and minimum isotropies,  $\alpha^* \equiv \min_{(u,v) \in D} \alpha(u,v)$ , of gnomonic map sets covering the sphere and generated from the platonic solids. It assumes triangular faces can be represented using triangular sampling arrays rather than embedded in a square:

Solid	$M_s$	$\alpha^*$	Components
tetrahedron	41.57	0.33	4
cube	24	0.58	6
octahedron	20.78	0.58	8
dodecahedron	16.65	0.79	12
icosahedron	15.16	0.79	20

Note that the sampling efficiency of dual equidistant maps is still better than the octahedral gnomonic map set. By using gnomonic maps derived from tessellations of more and more faces, we can approach but never attain the sampling requirement of an isometric map of  $4\pi$ . Using more than a few map components greatly complicates the projection function (i.e., texture coordinate generation) as well as efficient texture access by hardware systems.

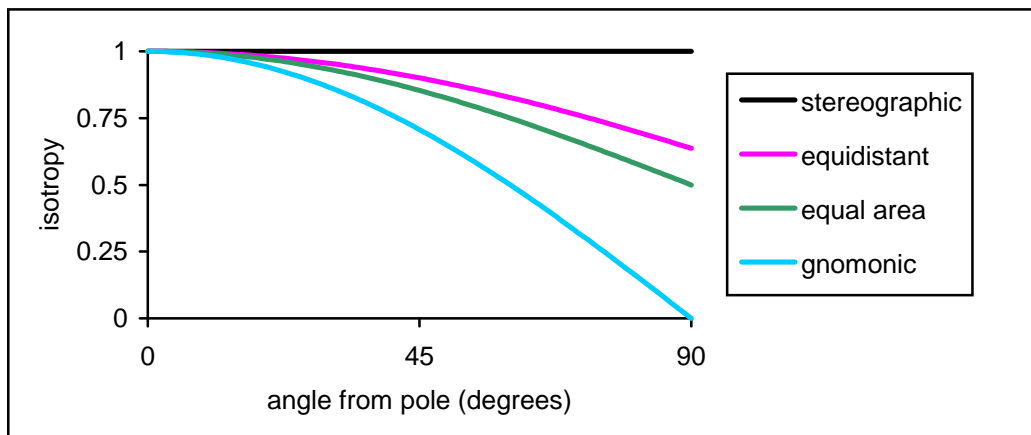


**Figure 8: Anisotropy of Azimuthal Maps as a Function of Angle from Pole.** Recall that isotropy values near 1 are desirable for hardware incapable of anisotropic filtering, values near 0 are undesirable.

Figure 8 graphs the anisotropy of the azimuthal projections. The stereographic map is best since it is conformal, but the equidistant map exhibits little anisotropy for angles less than about  $45^\circ$ , where its isotropy is  $\alpha(\pi/4) = 2\sqrt{2}/\pi \approx 0.9$ . This can be compared to its still reasonable isotropy at the equator,  $\alpha(\pi/2) = 2/\pi \approx 0.64$ . Gnomonic maps have worst-case anisotropy at the greatest angular distance from the pole. For example, the cube map has worst case isotropy of  $1/\sqrt{3} \approx 0.58$  at the cube vertices.

<sup>2</sup> This analysis contradicts an implication in [Hei99] that the dual stereographic projection is superior to the cube face map for sampling efficiency. [Hei99] correctly observes that the differential area for the stereographic map in a hemisphere varies by a factor of 4, while for the cube map it varies by more than a factor of 5 over the face. While true, this is less important than the factor of 2 greater spectral stretch at the pole generated by the stereographic compared to the gnomonic projection. The inefficient use of domain area by the cube map takes place over the relatively small corner regions; in total it is still 25% more efficient than the dual stereographic map.

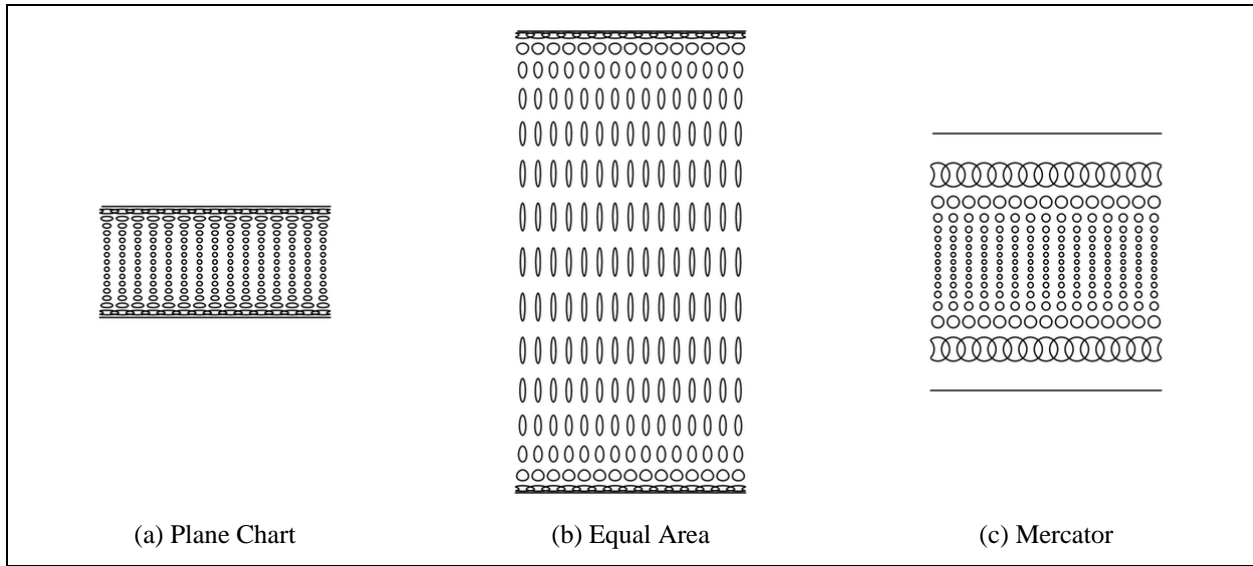


**Figure 9: Cylindrical Projections:** Spherical circles are distributed as defined in Figure 5, and projected into the parameter space of the three cylindrical mappings.  $u$  values are charted horizontally and  $v$  values vertically. Note that the Mercator projection has an unbounded domain in  $v$ , but only the spherical area very close to the poles is greatly stretched: the  $3.5^\circ$  spherical circles surrounding the poles map to the horizontal lines shown at the top and bottom.

### 3.2 Cylindrical Projections

Cylindrical projections transform the sphere to a tangent or intersecting cylinder such that parallels are projected to straight lines, with the model

$$\mathbf{S}(u, v) = (\cos(2\pi u)\cos\theta(v), \sin(2\pi u)\cos\theta(v), \sin\theta(v)), \quad u \in [-1/2, 1/2], \quad \theta(v) \in [-\pi/2, \pi/2]$$

where  $\theta(v)$  arbitrarily reparameterizes the parallel spacing, and where  $\theta = -\pi/2$  and  $\theta = \pi/2$  represent the poles, and  $\theta = 0$  the equator. Three important cylindrical projections, the plane chart, equal area, and Mercator projection, are illustrated in Figure 9 with mathematical properties tabulated in Figure 10.

The *plane chart* is the standard latitude/longitude parameterization of the sphere. It is also stretch-preserving. As its name implies, the *equal area* cylindrical projection preserves area. Finally the *Mercator* projection is a conformal projection useful for navigation since it projects *loxodromes* on the sphere, or curves making a constant angle with the meridians, into straight lines. Since all cylindrical projections are orthogonal, their spectral stretch is identical to their larger singular value, simplifying the analysis of sampling efficiency.

	Plane Chart	Equal Area	Mercator
$\theta(v)$	$2\pi v$	$\sin^{-1} v$	$\sin^{-1}(\tanh(2\pi v))$
properties	stretch-preserving	area-preserving	conformal
$v$ covering sphere	$[-1/4, 1/4]$	$[-1, 1]$	$[-\infty, \infty]$
$v(\theta)$	$\theta/(2\pi)$	$\sin\theta$	$\tanh^{-1}(\sin\theta)/(2\pi)$ $= \ln((1 + \sin\theta)/(1 - \sin\theta))/(2\pi)$
$\cos\theta$	$\cos(2\pi v)$	$\sqrt{1 - v^2}$	$\operatorname{sech}(2\pi v)$ $= 2/(e^{2\pi v} + e^{-2\pi v})$
$\sin\theta$	$\sin(2\pi v)$	$v$	$\tanh(2\pi v)$ $= (e^{2\pi v} - e^{-2\pi v})/(e^{2\pi v} + e^{-2\pi v})$
$\lambda_1(\theta)$	$2\pi$	$\max(1/\cos\theta, 2\pi\cos\theta)$	$2\pi\cos\theta$

$\lambda_2(\theta)$	$2\pi \cos \theta$	$\min(1/\cos \theta, 2\pi \cos \theta)$	$2\pi \cos \theta$
$\alpha(\theta)$	$\cos \theta$	$\min(1/(2\pi \cos^2 \theta), 2\pi \cos^2 \theta)$	1
$\tau(\theta)$	$4\pi^2 \cos \theta$	$2\pi$	$4\pi^2 \cos^2 \theta$
$\lambda_1^*(\theta)$	$2\pi$	$\max(1/\cos \theta, 2\pi)$	$2\pi$
$M_S(\theta)$	$2\pi\theta$	$\max(1/\cos^2 \theta, 4\pi^2) \sin \theta$	$2\pi \tanh^{-1}(\sin \theta)$ $= \pi \ln((1 + \sin \theta)/(1 - \sin \theta))$
inverse map	$u = (\text{atan } 2(y, x))/(2\pi)$ $v = (\sin^{-1} z)/(2\pi)$	$u = (\text{atan } 2(y, x))/(2\pi)$ $v = z$	$u = (\text{atan } 2(y, x))/(2\pi)$ $v = \tanh^{-1} z/(2\pi)$ $= \ln((1+z)/(1-z))/(4\pi)$

**Figure 10: Table of Mathematical Properties of Cylindrical Projections.** The maximum singular value and sampling requirement are taken over the part of the sphere from  $[0, \theta]$ ; i.e., from the equator to the  $\theta$  parallel. Local properties of the cylindrical projections are invariant with respect to  $u$ , depending only on  $v$  or inverting,  $\theta$ .

To analyze sampling efficiency, we consider the portion of the sphere from the equator to an angle  $\theta \leq \pi/2$ . The sampling requirement tabulated in Figure 10 and graphed in Figure 11 is given by

$$M_S(\theta) = v(\theta) \lambda_1^*(\theta) \quad \text{where}$$

$$\lambda_1^*(\theta) = \max_{\varphi \in [0, \theta]} \lambda_1(\varphi)$$

since the domain area is equal to  $v(1/2 - -1/2) = v$ . The plane chart is most sampling-efficient because it is stretch-invariant, just as the equidistant map is best among azimuthal projections. Covering the hemisphere using the plane chart has sampling requirement  $M_S(\pi/2) = 2\pi(\pi/2) \approx 9.87$ , identical to that of the azimuthal equidistant map. The other two maps have unbounded sampling requirement for hemispherical coverage. The cylindrical equal area map in fact has very poor sampling efficiency for any angular coverage, while the Mercator projection, at least for angles not more than about  $45^\circ$ , is only slightly worse than the plane chart, with the advantage of conformality.

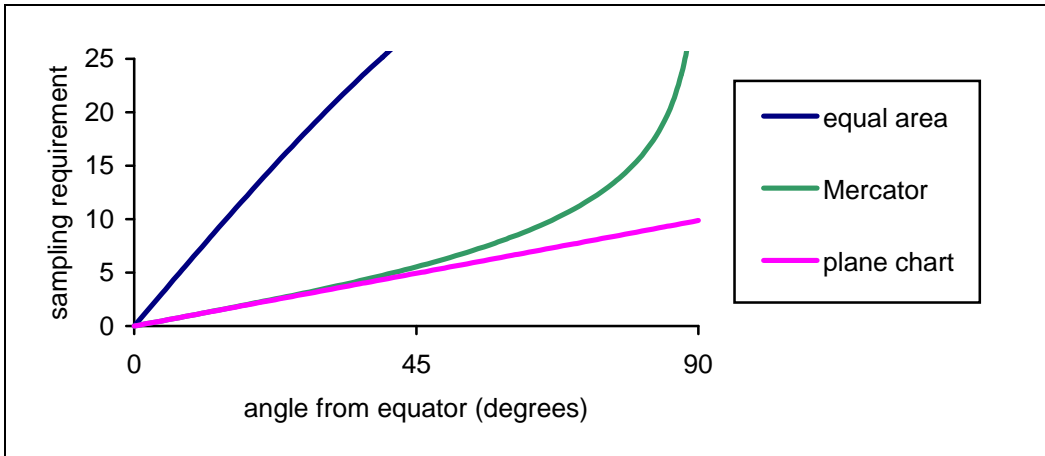


**Figure 11: Sampling Requirements of Cylindrical Maps as a Function of Angular Coverage.**

Anisotropy of the cylindrical maps is graphed in Figure 12. Note that for small angles from the equator, the plane chart exhibits little anisotropy, but its anisotropy increases without bound near the pole making it a poor choice for MIPMAP texturing. At  $45^\circ$ , the plane chart has isotropy  $\alpha(\pi/4) = \sqrt{2}/2 \approx 0.71$ . The area-preserving map has poor anisotropy (except near the single value  $\theta = \cos^{-1}(1/\sqrt{2\pi}) \approx 66.5^\circ$ ) as well as sampling efficiency.

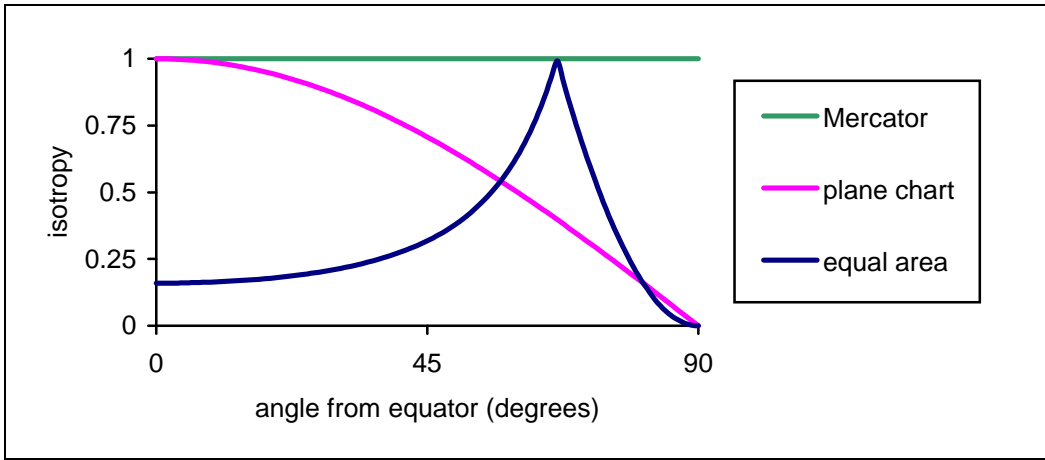


Figure 12: Anisotropy of Cylindrical Maps as a Function of Angle from Equator.

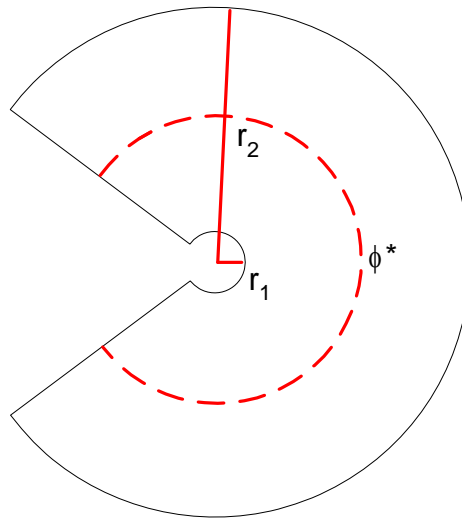


Figure 13: Equidistant Cone Domain: The specific shape is for  $\rho = \pi/4$ .

### 3.3 Conical Projections

A third major class of projections used in cartography are the *conical* projections. One specific type uses a cone tangent to the sphere at some parallel,  $\rho$ , projecting parallels to rings around the cone, and then isometrically to a planar sector of an annulus (Figure 13).<sup>3</sup> As is the case for azimuthal and cylindrical projections, the most sampling efficient projection is equidistant; that is, having equally spaced parallels. The mapping domain's annulus sector has inner radius  $r_1 \equiv \tan \rho - \rho$ , outer radius  $r_2 \equiv \tan \rho + \pi/2 - \rho$ , and sector angle  $\phi^* \equiv 2\pi \cos \rho$ . The parallel  $\rho$  projects to the arc with radius  $\tan \rho$ . The map is given by

$$\mathbf{S}(u, v) = (\cos(\phi \sec \rho) \sin \theta, \sin(\phi \sec \rho) \sin \theta, \cos \theta)$$

where  $\phi \equiv \text{atan} 2(v, u)$ ,  $\theta \equiv r - (\tan \rho - \rho)$ , and  $r \equiv \sqrt{u^2 + v^2}$ . This mapping is stretch-invariant and generalizes the azimuthal equidistant ( $\rho \rightarrow 0$ ) and plane chart projections ( $\rho \rightarrow \pi/2$ ).

<sup>3</sup> Note that a cone of half-angle  $\alpha/2 = \pi/2 - \rho$  can be isometrically mapped from a sector of angle  $\phi^* = 2\pi \sin \alpha/2 = 2\pi \cos \rho$ . The degenerate equidistant cones tangent at the pole (plane) or equator (cylinder) yield in the limit the azimuthal equidistant and plane chart projections, respectively.

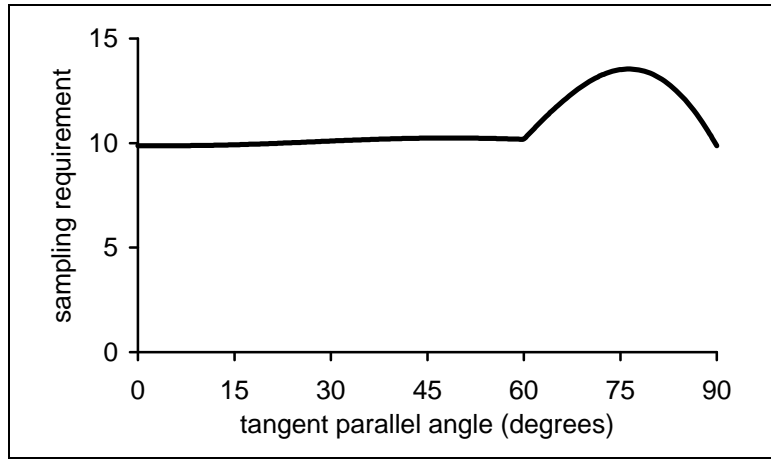


**Figure 14: Conical Equidistant Sampling Efficiency For Rectangular Embedding** as a function of tangent parallel latitude from pole. Note that the twin minima at  $\rho = 0^\circ$  and  $\rho = 90^\circ$ .

Without considering the embedding of its domain into a square (i.e., only its intrinsic area), it can be shown that the most sampling-efficient equidistant conical projection has  $\rho = 45^\circ$  with sampling requirement for hemispherical coverage of  $\pi^2 \sqrt{2}/2 \approx 6.98$ . This is better than the azimuthal equidistant<sup>4</sup> ( $\pi^2 (\pi/4) \approx 7.75$ ) and plane chart ( $\pi^2 \approx 9.87$ ). The shape of the domain for this mapping is shown in Figure 13. Unfortunately, once the map is embedded in a square it becomes significantly less efficient ( $(2r_s)^2 = 4(1 + \pi/4)^2 \approx 12.57$ ) than either the square-embedded azimuthal or plane chart projections. Moreover, no other  $\rho \notin \{0, \pi/2\}$  improves sampling efficiency, considering its rectangle-embedded area, as shown by the graph in Figure 14.

### 3.4 Low-Distortion Area-Preserving Map

We also present results for an unusual sphere mapping developed for use in a stochastic ray tracer. This mapping was designed to project stratified sampling patterns (and other specialized sampling patterns) onto the sphere and to project spherical samples into 2D histogram bins. To solve those problems, the mapping had to be a bijection between the unit square and the unit sphere, area-preserving, and not severely anisotropic. Its projection,  $(u, v) = \mathbf{S}^{-1}(x, y, z)$ , is defined by the composition of three area-preserving bijections. The first is a mapping from a hemisphere to a disk:

$$(u, v) = (x, y) / \sqrt{1 + z}$$

The second mapping is from a disk to a half disk:

$$(r', \theta') = (r, \theta/2)$$

Thus the two halves of a sphere are converted into half disks, which are joined to form a single disk. The third mapping is Shirley's area-preserving bijection between the disk and the unit square [Shi97]. This leaves us with an image of the sphere on the unit square, where the north and south pole are both mapped to the center of the square. If we roll the mapping halfway, the north pole will be on one edge of the square, the south pole on the opposite edge, and the interior of the square will be  $C_0$  continuous. See Figure 15d for the mapping applied to the image of the earth.

Numerical analysis of this mapping shows the sampling efficiency to be about 19.7, about the same as plane chart and dual equidistant mappings. Its worst-case isotropy is about 0.29.

## 4 Polar-Capped Maps

Azimuthal and cylindrical projections are complimentary, in that azimuthal projections tend to have better sampling efficiency and less anisotropy near the pole, while cylindrical projections are better near the equator. We can therefore improve both sampling efficiency and anisotropy by employing a three-component map set that uses an azimuthal projection for each of the two poles and a cylindrical projection near the equator. We call such a map a *polar-capped map* and analyze the properties of two variants in the next sections. Note that multi-component maps are analogous to the idea of *interrupted maps* from cartography.

<sup>4</sup> This number is different than the sampling efficiency stated in Section 3.1 since we no longer embed the domain in a bounding square.

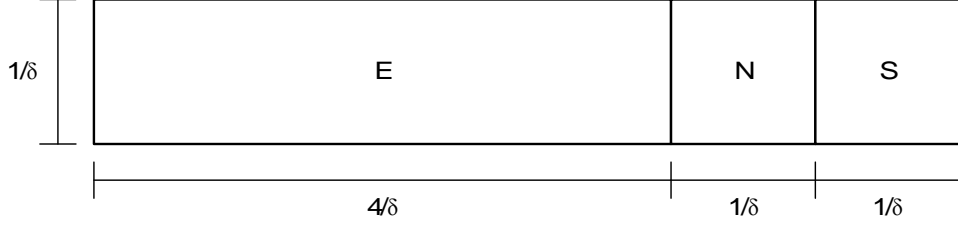


**Figure 15: Stretch-Invariant Polar-Capped Map:** The rectangle E represents the plane chart equatorial map, whose vertical resolution matches that of the two azimuthal equidistant polar caps, labeled N and S. Such a map with sample spacing  $\delta$  produces a minimum sampling spectral radius of  $\Delta^* = 2/\delta$ , for a sampling requirement of  $(3/2)\pi^2 \approx 14.8$ .

#### 4.1 Stretch-Invariant

To create an optimal stretch-invariant polar-capped map, we examine the sampling requirement of a two-component map covering the hemisphere, containing a plane-chart projection near the equator and an azimuthal equidistant projection near the pole. The sampling requirement of such a map is given by

$$M_{\text{capped}}(\theta) \equiv M_{\text{equi}}(\theta) + M_{\text{plane}}(\pi/2 - \theta) = 4\theta^2 + 2\pi(\pi/2 - \theta)$$

where  $\theta$  is the angle from the pole where the equidistant projection transitions to the plane chart. We seek  $\theta$  minimizing the sampling requirement. Differentiating and finding the root, it is easy to see that the sampling-requirement minimizing angle occurs at  $\theta^* \equiv 45^\circ$  for which the sampling requirement is  $3/4 \pi^2 \approx 7.40$ . To cover the entire sphere, we can therefore continue the equatorial map to the southern hemisphere and add a third equidistant map covering the south pole to produce a polar-capped map with sampling requirement of roughly 14.80. This represents an improvement of 54% over the dual stereographic map, 38% over the cube map (but with half as many map components and much less anisotropy), and 25% over the dual equidistant or plane chart maps (but with much less anisotropy). It is even a slight improvement (2.4%), over the unwieldy 20-map icosahedral gnomonic set!

We next analyze the structure of the polar-capped map's domain. The domain for each of the two polar caps is  $[-1/2, 1/2] \times [-1/2, 1/2]$  since  $r(\theta^*) = 1/2$ , while the equatorial map's domain is  $[-1/2, 1/2] \times [-1/8, 1/8]$  since  $v(\pi/2 - \theta^*) = 1/8$ . To find the respective sampling densities, the sampling spectral radius must be equal on the three maps. But  $\Delta^*/\pi = 1/(\Gamma^* \delta)$ ,  $\Gamma_{\text{equi}}^* = \pi/2$ , and  $\Gamma_{\text{plane}}^* = 2\pi = 4\Gamma_{\text{equi}}^*$  so  $\delta_{\text{plane}} = 1/4 \delta_{\text{equi}}$  to match spectral radii. Thus the resolution of the two polar caps is  $1/\delta \times 1/\delta$  and the equatorial map is  $4/\delta \times 1/\delta$  to achieve a minimum sampling spectral radius of  $\Delta^* = 2/\delta$ . It can be seen that the three maps share a common resolution in the second ( $v$ ) dimension, and so can be adjoined to form a contiguous rectangle with aspect ratio  $6 \times 1$ , as shown in Figure 15. The map achieves minimum (worst-case) isotropy of  $\alpha^* = \sqrt{2}/2 \approx 0.71$  which occurs at the  $45^\circ$  parallel of the plane chart. Note also that aspect ratios of the three maps are either square, or  $4 \times 1$ , and so are supported on hardware with the "powers of 2" constraint on texture resolution.

#### 4.2 Conformal

While the stretch-invariant polar-capped map has little anisotropy (the worst case is  $\alpha \approx .71$  at the  $45^\circ$  parallel of the plane chart), it is instructive to compare another version which is conformal everywhere. The best conformal polar-capped map is constructed by combining stereographic maps at the poles with a Mercator projection at the equator. Such a map has sampling requirement

$$M_{\text{capped}}(\theta) \equiv M_{\text{stereo}}(\theta) + M_{\text{Mercator}}(\pi/2 - \theta) = 16 \tan^2(\theta/2) + \pi \ln((1 + \cos \theta)/(1 - \cos \theta))$$

where  $\theta$  is, as before, the transition angle. The optimal angle occurs occurs at

$$\theta^* = \cos^{-1}((1 - \pi/16)/(1 + \pi/16)) \approx 47.8^\circ$$

for which the sampling requirement is  $\pi(1 + \ln(16/\pi)) \approx 8.26$ . The entire sphere can then be covered with three maps with a sampling requirement of 16.51, an 11.6% increase over the stretch-invariant polar-capped map to obtain local isotropy everywhere.

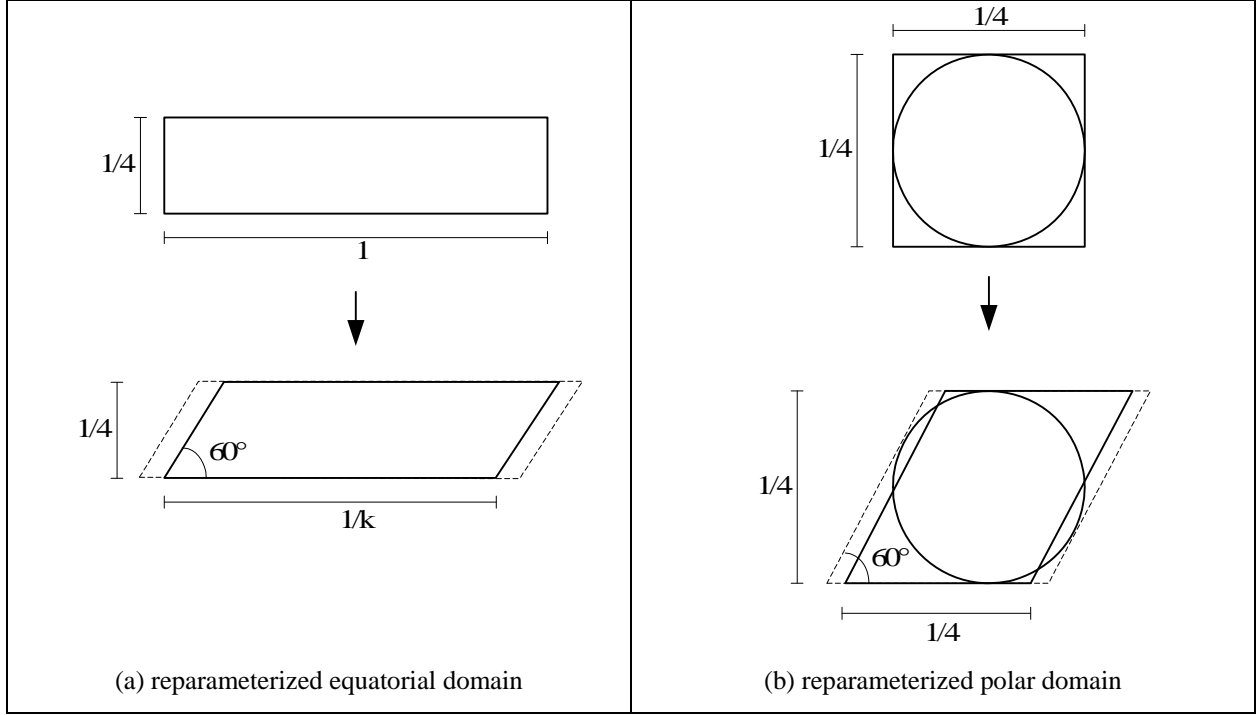


**Figure 16: Hexagonal Reparameterization of the Polar-Capped Map.** In (a), the equatorial map is hexagonally reparameterized using a  $60^\circ$  shear, resulting in a reduction of domain area by a factor of  $k$ . The technique is useless for the polar caps (b), because the domain area needed to contain the disk increases to exactly counteract the savings.

### 4.3 Hexagonally Reparameterized

The stretch invariant polar-capped map can be further improved by distorting the rectangular sampling lattice into the optimal hexagonal one. This is easily accomplished by transforming the input of the mapping function through a constant linear transformation

$$\hat{\mathbf{S}}(u, v) \equiv \mathbf{S}(\mathbf{V}(u, v)')$$

where

$$\mathbf{V} \equiv \begin{bmatrix} k & k/2 \\ 0 & 1 \end{bmatrix}$$

and  $k \equiv 2\sqrt{3}/3$  as in Section 2.3. The sampling matrix  $\mathbf{V}$  here is another variant of hexagonal sampling (compare to  $\mathbf{V}_{hex}$  Section 2.1).

Since the plane chart mapping is orthogonal, it can be shown that  $\hat{\mathbf{S}}$  preserves the spectral stretch of  $\mathbf{S}$ . Also, since the plane chart is periodic in  $u$ , the domain required by  $\hat{\mathbf{S}}$  to cover the hemisphere becomes  $[-1/(2k), 1/(2k)] \times [-1/8, 1/8]$ , resulting in a reduction of domain area, and hence sampling requirement, by a factor of  $k$  due to the reduction in  $u$  samples. Less advantageous is the effect of this reparameterization on the anisotropy of  $\hat{\mathbf{S}}$ , which now achieves a minimum isotropy of  $\alpha^* = 1/\sqrt{3} \approx 0.58$ , somewhat worse than  $\mathbf{S}$ . While it would seem that the hexagonal reparameterization could be done in either the  $u$  or  $v$  dimension, reducing sampling density in  $u$  is a better choice. This is because compressing  $v$  exacerbates the anisotropy already present in the  $45^\circ$  parallel, reducing  $\alpha^*$  still further, whereas compressing  $u$  actually improves anisotropy there.<sup>5</sup>

<sup>5</sup> Note that the worst-case anisotropy of  $\hat{\mathbf{S}}$  is actually achieved at the equator.

Unfortunately, while this technique improves the equatorial map’s sampling efficiency, it is useless on the polar caps. The reason for this is that the new domain must still cover the disk of radius  $1/2$ . Fitting this disk into the sheared domain requires an increase in area that exactly counteracts the reduction in sampling density, resulting in no savings (Figure 16). This is an essential limitation of the rectangular sampling lattice.

We therefore hexagonally reparameterized only the equatorial map. Since this map uses  $2/3$  of the samples (refer to Figure 15), we achieve a sampling requirement of

$$\left(3\pi^2/2\right)\left(\frac{2}{3k} + \frac{1}{3}\right) \approx 13.48$$

a savings of about 9% over the stretch invariant polar-capped map. Note that this additional sampling efficiency is only realizable on graphics hardware that supports arbitrary sampling aspect ratios in texture rectangles, rather than powers of 2.

## 5 Results

Figure 15 illustrates five texture maps of the earth with identical texture area: stretch-invariant polar-capped (a), gnomonic cube (b), dual stereographic (c), low distortion area preserving (d), and Lambert equal area (e). Note particularly the sizes of various features such as the polar ice caps. For example, it can be seen that the gnomonic cube (Figure 15a) shrinks Anarctica, and thus will sample that area less effectively than the polar-capped map (Figure 15b). The dual stereographic map (Figure 15c) reduces Anarctica still further.

Figure 16 compares the maps using a high-frequency test pattern on the sphere. This pattern is first sampled into texture maps of identical area for each of the 5 example maps. We then generate orthographic views of the sphere textured with each of these results, shown in the top row. We chose a view where the south pole has been rotated towards the viewer by  $45^\circ$  so that both polar and equatorial regions are visible. The row below zooms in on the south pole of the row above which represents a “bad spot”, or most undersampled region, for each of the maps.<sup>6</sup>

Our sampling efficiency metric is based on worst-case frequency preservation using the principle that all parts of the sphere must be sampled well to avoid visual artifacts. The bottom row of Figure 16 validates the mathematical ranking of the maps which decrease in sampling efficiency from left to right. Discriminating between the low distortion equal area (LDEA) map and the gnomonic cube is difficult. This is probably because we applied the spherical texture using bilinear filtering to simulate typical graphics hardware, which penalizes the more highly anisotropic LDEA map. The top row shows the polar-capped map’s sharpness uniformity over the entire sphere. The other maps have noticeable patches of blurriness near the south pole.

## 6 Conclusions and Future Work

Mapping functions used to represent spherical images in graphics systems are much less than optimal in terms of sampling efficiency. This paper formally defines the notion of sampling efficiency and analyzes existing and new maps in terms of sampling efficiency and local anisotropy. Our analysis finds that some commonly used maps, like OpenGL’s have problems with sampling efficiency. The familiar latitude/longitude (plane chart) parameterization has the best sampling efficiency among maps commonly used before, but it suffers from unbounded anisotropy making it undesirable for graphics hardware. We introduce pieces of projections used in cartography to form two- and three-component maps that have better sampling efficiency than the best map used previously, with little or no anisotropy. For example, the stretch invariant polar-capped map saves 54% over the dual stereographic map, 38% over the cube map, and 25% over the latitude/longitude map with minimal anisotropy handled by existing hardware. Moreover, no map, regardless of the number of its components, can exceed its efficiency by more than 26%, and even the 20-component, icosahedral gnomonic set is inferior. Implementation involves replacing the texture coordinate generation function with a simple alternative.

We believe the sampling efficiency metric can be extended to Monte Carlo integration for rendering. Stratified stochastic sampling seeks to scatter as few samples as possible to arrive at an integral estimate with greatest confidence, and often uses global mapping functions from simple domains to simplify sampling [Arv95,Mit96]. While area-preserving mappings like [Arv95] assure that all samples contribute equally to the integral estimate, maps with a great deal of local stretch, a typical consequence of area-preserving mapping to surfaces with curvature, increase variance (i.e., reduce the effectiveness of stratification). How should these considerations be balanced? A surface integral of spectral stretch, rather than a simple maximum, may be the right comparison metric for mappings used for integrating rather than tabulating functions over surfaces.

<sup>6</sup> The polar-capped map has no bad spot. The other maps have bad spots at both poles or at the south pole (Lambert).

## 7 References

- [Arv95] Arvo, J., "Stratified Sampling of Spherical Triangles," *Siggraph '95*, August 1995, 437-438.
- [Bli76] Blinn, J.F., and M.E. Newell, "Texture and Reflection in Computer Generated Images", *Communications of the ACM*, 19(10):542-547, October 1976.
- [Bri56] Brillouin, L., *Science and Information Theory*, Academic Press, 105-111, 1956.
- [Cab99] Cabral, B., M. Olano, and P. Nemeč, "Reflection Space Image Based Rendering," *Siggraph '99*, August 1999, 165-170.
- [Che95] Chen, Shenchang, "QuickTime VR – An Image-Based Approach to Virtual Environment Navigation", *Siggraph '95*, August 1995, 29-38.
- [Dud84] Dudgeon, Dan, and R. Mersereau, *Multidimensional Digital Signal Processing*, Prentice Hall, 1984.
- [Fiu87] Fiume, E., A. Fournier, and V. Canale, "Conformal texture mapping", *Proc. of EUROGRAPHICS '87*, Elsevier Science Publishers (North Holland), Amsterdam (1987), 53-64.
- [Gre86] Greene, N., "Environment Mapping and other Applications of World Projections," *Computer Graphics and Applications*, 6(11):21-29, November 1986.
- [Hae93] Haeberli, P., and M. Segal, "Texture Mapping as a Fundamental Drawing Primitive," in *Fourth Eurographics Workshop on Rendering*, June 1993, 259-266.
- [Hei99] Heidrich, Wolfgang, and H.P. Seidel, "Realistic, Hardware-Accelerated Shading and Lighting," *Siggraph '99*, August 1999, 171-178.
- [Hüt99] Hüttner, T., and W. Straßer, "Fast Footprint MIPmapping," in *Proceedings 1999 Eurographics/Siggraph Workshop on Graphics Hardware*, Aug. 1999, 35-43.
- [Mil98] Miller, G., M. Halstead, and M. Clifton, "On-the-fly Texture Computation for Real-Time Surface Shading," *IEEE Computer Graphics and Applications*, March 1998, 44-58.
- [Mit96] Mitchell, D., "Consequences of Stratified Sampling in Graphics," *Siggraph '96*, August 1996, 277-280.
- [Ope92] *OpenGL Reference Manual*, Addison Wesley, 1992.
- [Pet62] Peterson, D.P., and D. Middleton, "Sampling and Reconstruction of Wave-Number Limited Functions in N-Dimensional Euclidean Spaces," *Information and Control*, 5(1962), 279-323.
- [Reg94] Regan, M. and R. Pose, "Priority Rendering with a Virtual Reality Address Recalculation Pipeline", *Siggraph '94*, 155-162.
- [Rob60] Robinson, Arthur, *Elements of Cartography*, John Wiley & Sons, New York, 1960.
- [Sch95a] Schröder, P., and W. Sweldens, "Spherical Wavelets: Efficiently Representing the Sphere," *Siggraph '95*, August 1995, 161-172.
- [Sch95b] Schröder, P. and W. Sweldens, "Spherical Wavelets: Texture Processing," in P. Hanrahan and W. Purgathofer, editors, *Rendering Techniques '95*, pp. 252-263, Springer Verlag, Wien, New York, 1995
- [Shi97] Shirley, Peter and Kenneth Chiu, "A Low Distortion Map Between Disk and Square", *Journal of Graphics Tools*, Vol 2, No 3, pp 45-52, 1997.
- [Sny93] Snyder, John P., *Flattening the Earth: Two Thousand Years of Map Projections*, The University of Chicago Press, London, 1993.
- [Voo94] Voorhies, Douglas, and Jim Foran, "Reflection Vector Shading Hardware," *Siggraph '94*, July 1994, 163-166.
- [Wil83] Williams, Lance, "Pyramidal Parametrics," *Siggraph '83*, July 1983, 1-11.



(a) Stretch-invariant Polar Capped



(b) Gnomonic Cube (Cube Map)



(c) Dual Stereographic



(d) Low Distortion Equal Area



(e) Lambert Equal Area (OpenGL)

Figure 15: Texture Maps of the Earth

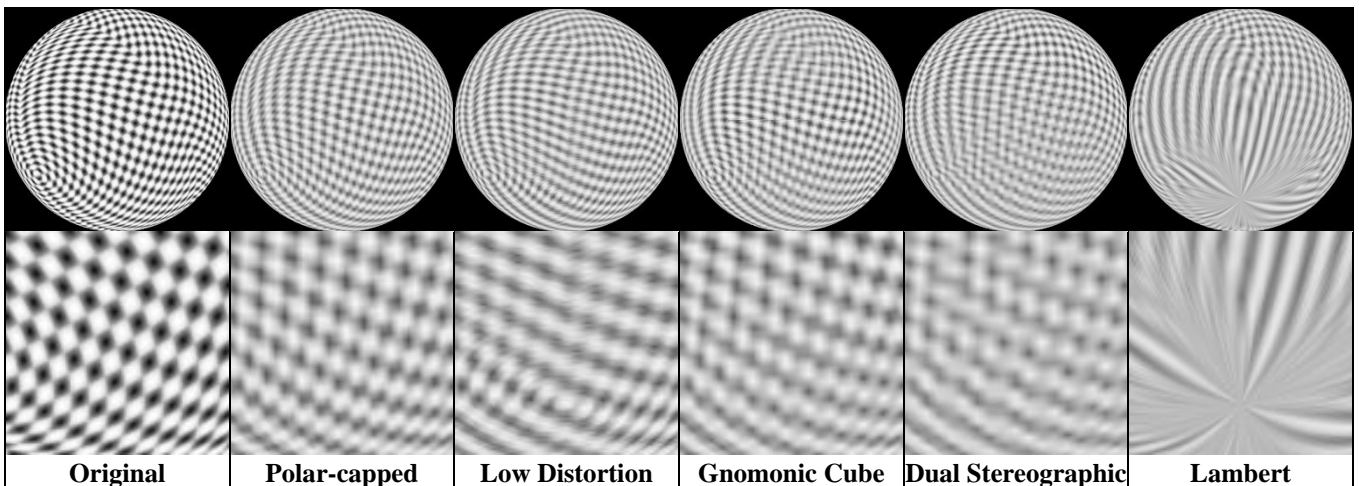


Figure 16: Results on Spherical Test Pattern

## 8 Appendix: Computing Spectral Stretch

Recall that the local sampling spectral stretch is given by

$$\Gamma^2(u, v) \equiv \frac{\tau^2(u, v)}{\min_{(n,m) \neq (0,0)} (\|n\mathbf{S}_u + m\mathbf{S}_v\|^2)} = \frac{ac - b^2}{\min_{(n,m) \neq (0,0)} (n^2a + 2nmb + m^2c)}$$

where  $a(u, v) \equiv \mathbf{S}_u \cdot \mathbf{S}_u$ ,  $b(u, v) \equiv \mathbf{S}_u \cdot \mathbf{S}_v$ , and  $c(u, v) \equiv \mathbf{S}_v \cdot \mathbf{S}_v$  are the entries in the symmetric metric tensor  $\mathbf{J}'\mathbf{J}$  as in Section 2.3. The minimization in this denominator can be found with a simple algorithm. For a fixed  $m$ , the denominator is minimized using (a non-integer)  $n^* = -mb/a$ . This can be easily seen by differentiating with respect to  $n$  and equating to 0.

Since the denominator is quadratic in  $n$  and  $c \geq 0$ , it increases symmetrically with increasing distance away from this minimum. Therefore, for a fixed  $m$ , the minimum length of the denominator over integer  $n$  is given by the closest integer to this minimum; i.e.,  $\tilde{n} = \lfloor n^* + 1/2 \rfloor$ . We can therefore try an increasing sequence of integers  $m$  starting from 1 and directly find the corresponding  $\tilde{n}$  that minimizes the squared length. The algorithm can be stopped when the minimum length for the  $n^*$  corresponding to the next  $m_i = m_{i-1} + 1$  is bigger than the minimum length already found. This is because this squared length, given by  $m^2(c - b^2/a)$ , necessarily increases as  $m$  increases, since  $ac - b^2 \geq 0$  and  $a, c \geq 0$ . The following algorithm implements these ideas.

```

/*
Returns min_{(n,m) != (0,0)} ||n u + m v ||^2
over n,m integers.

Rather than supplying u and v directly, must supply:

    a = u.u
    b = u.v
    c = v.v

Assumes u and v are nondegenerate vectors (nonzero length
and linearly independent).
*/
double min_linear_comb_over_lattice(double a,double b,double c)
{
    double minlensq = MIN(a,c);
    double rsq,l;
    int m,msq;

    if (a > c) { /* swap to maximize usefulness of each iteration */
        double tmp = a;
        a = c;
        c = tmp;
    }

    l = -b/a;
    rsq = c + l*l*b;

    m = 1;
    msq = 1;
    while (msq*rsq <= minlensq) {
        double bestn = floor(m*l+0.5);
        double lensq = msq*c + bestn*(2*m*b + bestn*a);

        minlensq = MIN(minlensq,lensq);

        m++;
        msq = m*m;
    }
    return minlensq;
}

```